Chemically monodispersed tin nanoparticles on monolithic 3D nanoporous copper for lithium ion battery anodes with ultralong cycle life and stable lithium storage

Wenbo Liu,[a,*] Xue Chen,[a] Peng Xiang,[a] Shichao Zhang,[b] Jiazhen Yan,[a] Ning Li,[a] Sanqiang Shi[c]

[a] School of Manufacturing Science and Engineering, Sichuan University, Chengdu 610065, China

[b] School of Materials Science and Engineering, Beihang University, Beijing 100191, China

[c] Department of Mechanical Engineering, The Hong Kong Polytechnic University, Hung Hom, Kowloon, Hong Kong

Tel: +86-028-85405320; Fax: +86-028-85403408; E-mail: liuwenbo_8338@163.com.

Abstract

In this report, a simple and effective low-temperature synthesis route has been proposed to smoothly achieve monodispersed tin nanoparticles upon monolithic 3D nanoporous copper (3D-NPC@MTNPs) from chemical dealloying of as-cast Al 45 at.% Cu alloy sheets in the HCl solution, which exhibits superior Li storage property and ultralong cycle life as anode for lithium ion batteries (LIBs). The results show that the 3D-NPC@MTNPs composite can be made massively by electroless plating Sn on uniform NPC matrix with pore size of ca. 200 nm in an acidic plating bath below room temperature. Compared to the two dimensional copper foil supported tin thin films (2D-CF@TTFs), the 3D-NPC@MTNPs electrode displays the markedly higher first reversible capacity of 0.485 mAh cm^{-2} as well as superior cycling stability with 52.4% capacity retention and over 96.7% coulombic efficiency after 500 cycles. This can be largely ascribed to the synergistic effect of favorable monodispersity of Sn nanoparticles with ultrafine particle size and single crystal feature as well as unique 3D nanoporous electrode architecture with large specific surface area and good mass transfer channel, which facilitates the accommodation of mechanical strain, improvement of structural stability, enhancement of bonding force, and acceleration of mass transfer, indicative of a quite promising candidate as high-performance anode for LIBs.

Keywords: *Lithium ion battery; Electroless plating; monodispersion; Porous substrate; Li storage property*

1. Introduction

Even though lithium ion batteries (LIBs) have been extensively applied in portable electronic devices and hybrid/pure electric vehicles, it still urgently demands great efforts to ameliorate the performance of components inside, such as specific capacity, cycle life, coulombic efficiency, rate capability and so forth.[1,2] As the commercial graphite anode material has nearly reached its theoretical limit (372 mAh g^{-1}), it is great important to develop new anode materials with higher capacity, such as metal based anode materials.[3,4] Tin, one of the most promising candidates, has attracted considerable attention due to its good electronic conductivity and high theoretical capacity (994 mAh g^{-1} for $Li_{4.4}Sn$), three times greater than commercial graphite.[5] However, such material is known to suffer from dramatic severe volume change (over 300% at its maximum) during lithiation-delithiation processes, which leads to quick cracking, pulverization and detachment of active material as well as fierce capacity degradation, thus hampering its further implementation in LIBs.[6-11]

The current strategies to overcome the pulverization and structure failure mainly include reducing the feature size of active material,[11-14] building active/inactive composite system,[7,15-16] and adopting 3D nanostructured current collector.[17,18] Typically, compared to the conventional 2D planar structure, the 3D porous substrates, such as carbon paper,[19] nickel network,[20,21] copper mesh configuration,[22,23] and metal cellular framworks,[24] possess several prominent merits as follows: (1) offering high-efficient electron transport path and favorable conductive environment for active materials; (2) accommodating large volume change and mechanical strains during

lithiation-delithiation processes; (3) providing more mass transfer channels for electrolyte and involved diffusion species.

Recently, nanoporous metals with quasiperiodic ligament/channel networks have been attempted to serve as both current collector and substrate of active materials for lithium ion battery anodes. For example, Yu et al. synthesized a 3D nanoporous gold (NPG) supported amorphous-Ge film anode with high specific capacity and good rate capability by dealloying and thermal evaporation.[25] Obviously, the production cost of NPG and complexity of preparation technology are quite high and far from commercialization; meanwhile, it could be considered that the morphology, size and distribution of active materials also should have a key influence on its electrochemical behavior. All of these inspired us to develop a simple and effective strategy to control them on nanoporous substrates from less noble metal families, despite of difficulties in ideal dispersion of active materials on 3D base metal matrix with high surface energy relative to noble one. As we know, electroless deposition as a conventional surface treatment approach has been widely applied to various industrial fields due to its evident advantages of simplicity, low cost and being applicable for large-scale production; however, its drawback is the limited controllability in morphology and distribution except for coating with a certain thickness.

Herein, we successfully achieve monodispersed tin nanoparticles with single crystal feature upon monolithic 3D nanoporous copper for lithium ion battery anodes without additional binder and conductive agents by skillful low-temperature electroless plating technique, which might be extended to use in production to make it

competitive in technology and economy. The freestanding 3D-NPC can be obtained readily by chemical dealloying of as-cast Al 45 at.% Cu alloy sheets in a diluted HCl solution, which can act as both current collector and substrate of tin simultaneously. Compared to the 2D-CF@TTFs, the 3D-NPC@MTNPs electrode displays the significantly improved first reversible capacity of 0.485 mAh cm^{-2} as well as excellent cycling stability with 52.4% capacity retention and over 96.7% coulombic effeciency after 500 cycles, which is likely associated with the synergistic effect between benign monodispersity of Sn nanoparticles with single crystal nature and unique 3D nanoporous electrode configuration with good mass transfer channel, suggesting a considerably promising application in high-performance LIBs.

2 Experimental

2.1. Preparation of 3D-NPC@MTNPs and 2D-CF@TTFs composites

Al-Cu alloy with nominal composition of 45 at.% Cu was prepared from pure Al (99.99 wt.%) and pure Cu (99.999 wt.%). Voltaic arc heating was employed to melt the charges in a copper crucible under an argon atmosphere, and then the melt was cooled down into ingots in situ. The Al-Cu ingots were sliced into sheets with 400 μm in thickness by wire-cutting EDM, which subsequently were ground and polished to remove oxide layers on the surfaces. Energy dispersive X-ray (EDX) analysis showed the atomic percentage of Cu and Al in the Al-Cu alloy sheets was quite closely to the designed composition, indicating the alloy sheets can be further used in the following study (see supplemental material for EDX results, Table S1). Afterwards, the Al-Cu alloy sheets were chemically dealloyed in a 5 wt.% HCl aqueous solution at 90℃ for

5 hrs. Upon dealloying, the samples were rinsed with distilled water and dehydrated alcohol for several times. The monolithic 3D-NPC was obtained after dried in a vacuum oven at 70℃ for 24 hrs. To further prepare the 3D-NPC@MTNPs, electroless deposition of Sn on NPC was conducted in a plating bath mainly containing 0.1 M $SnSO_4$, 1 M thiourea, 0.5 M sodium hypophosphite and 0.85 M concentrated sulfuric acid at a low temperature (~5℃) for a relatively short time in order to control the nucleation and growth processes of Sn on NPC. The typical deposition time ranges from 5 to 10 s. The preparation flow of the 3D-NPC@MTNPs was illustrated schematically in Fig. 1. For comparison, the 2D-CF@TTFs composite also was fabricated by electroless deposition onto 2D copper foil (2D-CF) substrate under the same conditions. Note that all areas in this work referred to foot print areas and all used chemical reagents were analytical grade.

2.2. Microstructure and composition characterization

Microstructural characterization and analysis of the initial Al-Cu alloy, as-prepared porous substrate and composite were performed using X-ray diffraction (XRD, Rigaku D/Max-2400) with Cu K_α radiation, scanning electron microscopy (FESEM, Hitachi S-4800) with an EDX analyzer, transmission electron microscopy (TEM, JEOL JEM 2100F).

2.3. Electrochemical test

Electrochemical charge-discharge behaviors were investigated in coin-type test cells (CR2032) assembled with the as-prepared 3D/2D composites, lithium foil and Celgard 2400 membrane in an Ar-filled glove box (LS-750D, DELLIX). Electrolyte

was 1M $LiPF_6$ in a mixed solution of EC and DEC (1:1 by v/v). Each half-cell was aged for 24 hrs at room temperature before commencing the electrochemical tests. The galvanostatic charge-discharge measurements were carried out in a multichannel battery test system (NEWARE BTS-610, Neware Technology Co., Ltd., China) for a cut-off potential of 0.01-1.5 V (vs. Li/Li^+) at ambient temperature. Cyclic voltammograms (CVs) was recorded using a CHI760E electrochemical workstation at a scan rate of 0.1 mV s^{-1} between 0.01 and 1.5 V (vs. Li/Li^+). Electrochemical impedance spectroscopy (EIS) measurements were carried out over a frequency range from 0.01 Hz to 1 MHz with AC amplitude of 5 mV.

The lithium ion full cell were assembled further by using the as-prepared 3D-NPC@MTNPs electrode without additional binder and conductive agents as anode and the conventional $LiCoO_2$ electrode as cathode, which was prepared by casting the slurry of 80 wt.% commercial $LiCoO_2$ power, 10 wt% polyvinylidene difluoride (PVDF) and 10 wt.% carbon black in N-Methyl-2-pyrrolidone (NMP) solvent on aluminium foil and then drying in a vacuum oven at 75℃ for 12 hrs. CR-2032 coin-type test cells were assembled in an Ar-filled glove box (H_2O<0.1 ppm, O_2<0.1 ppm; LS-750D, DELLIX). Celgard 2400 microporous poly-propylene film was used as the separator membrane and 1 M $LiPF_6$ was dissolved in a mixed solution of EC and DEC in a volume ratio of 1:1 as the electrolyte. The electrochemical performance of the assembled full cells was tested on a multichannel battery test system (NEWARE BTS-610, Neware Technology Co., Ltd., China) at a voltage range of 1.0-3.8 V after aging for 24 hrs at room temperature.

3. Results and discussion

Fig. S1 shows the XRD pattern of the initial Al 45 at.% Cu alloy sheets. It is clear that the initial alloy is composed of Al_2Cu and AlCu phases, in which the AlCu is predominant in the alloy based on their relative peak intensities. Fig. 2 displays the XRD patterns of the as-dealloyed sample and related composite upon low-temperature electroless plating tin, respectively. As can be seen from Fig. 2a, only a face-centered cubic (f.c.c.) Cu phase can be identified in the as-dealloyed samples under the X-ray detection limit. After the electroless deposition, it can be found that there exist two phases involving the original f.c.c. Cu as well as deposited tetragonal β-Sn. Similarly, the f.c.c. Cu and β-Sn phases also can be detected simultaneously in the resultant 2D-CF@TTFs composite by electroless plating tin onto 2D-CF substrate under the same conditions (Fig. S2). Note that the minor Cu_6Sn_5 appears in the XRD pattern probably due to the interaction between Cu and Sn atoms at their interfaces caused by diffusion. The present outcomes clearly indicate that tin has been successfully loaded onto the as-dealloyed 3D-NPC and 2D-CF substrates by low-temperature electroless deposition.

The plane view of the as-dealloyed samples from Al 45 at.% Cu alloy shows a uniform porous structure upon dealloying in the acidic solution and one typical SEM image is presented in Fig. 3a. The surface micromorphology at a higher magnification exhibits an open, bicontinuous interpenetrating network structure with dramatically larger ligament sizes of ca. 500 nm as compared to the pore dimensions (ca. 200 nm, Fig. 3b), which could be greatly beneficial for follow-up deposition of active material

and its controllability in morphology and dispersity. The EDX result shows only Cu can be identified and nearly all of Al was etched away during dealloying by the acidic solution (inset of Fig. 3a). Intriguingly, NPG substrate by dealloying of prototypical Ag-Au alloys normally contains some residual at.% Ag, which cannot be removed but asymptotically reaches a limit at quite long etching times (up to 100 hrs).[26,27]

Fig. 3c-d displays the typical SEM images of 3D composite after low-temperature electroless plating tin on 3D-NPC substrate. Obviously, ultrafine tin nanoparticles just with several nm in diameter dispersed on the ligaments of NPC uniformly; meanwhile, an open, bicontinuous interpenetrating porous network morphology, quite similar to the original 3D-NPC, can be well preserved in the resultant composite after the electroless deposition. Additionally, EDX analysis has been carried out on the composite, and compared to that of 3D-NPC substrate, Sn and Cu can be detected simultaneously in the 3D composite, implying tin has been deposited successfully on NPC substrate. For comparison, tin also has been loaded on the 2D-CF substrate under the similar condition and uniform tin thin films with typical thickness of ca. 4 μm can be observed clearly after the electroless plating, as illustrated in Fig. 3e and Fig. S2. It should be noted, however, that the high-magnification SEM image (Fig. 3f) exhibits that the tin thin films still comprising the large number of compactly stacking nanoparticles with characteristic sizes of 250±50 nm, just greater than those in the 3D composite. It is worthwhile noting that the present findings are quite different from smooth tin coatings or significantly large tin particles obtained usually under similar deposition conditions at the typical industrial deposition temperature of room

temperature (or higher) in the previous literature.[28-31] As a result, we can conclude that the morphology, size and dispersity of Sn can be adjusted and controlled effectively by changing its kinetic nucleation and growth processes via the simple low-temperature electroless deposition.

TEM observation further verifies the favorable dispersity of Sn on NPC substrate, which is well consistent with the SEM results and a typical TEM bright-field image is displayed in Fig. 3g. Clearly, the monodispersed Sn nanoparticles with feature sizes of 6±2 nm can be observed on the ligaments of NPC after the electroless deposition, resulting in the formation of ideal 3D-NPC@MTNPs composite. It is worth noting that the smaller particle size and more uniform dispersity can be obtained easily in the 3D-NPC@MTNPs composite compared with that in the 2D-CF@TTFs one, which is likely related to the large specific surface area and unique surface microenvironment (curvature, roughness and unsaturated bond) of 3D-NPC substrate. Moreover, the HRTEM observation shows different lattice fringes with interplanar spacings of 0.292 nm and 0.209 nm, assigning to the (200) reflection of Sn phase and the (111) reflection of Cu phase, respectively. A clear boundary between Cu substrate and Sn nanoparticles can be distinguished readily based on their different lattice orientations, as marked by broken line in Fig. 3h. Note that the lattice fringes from Sn extending throughout the whole nanoparticle indicate its single crystal nature. Due to the temperature-dependent thermal activation process and insufficient reaction time, the nucleation and growth of Sn on the 3D-NPC substrate can be managed skillfully. This probably is why tin can be deposited in the form of single-crystal nanoparticles rather

than smooth thin films by the electroless plating at the low temperature in this work.

Subsequently, the as-synthesized unique 3D-NPC@MTNPs composite was further attempted to act as a binder-free anode for LIBs to evaluate its superiority in energy storage device. For the typical Sn-based electrode, as well-known, the electrochemical lithiation/delithiation processes mainly include two reaction steps as follows:[32-34]

$$Sn + xLi^+ + xe^- \rightarrow Li_xSn \quad (0 < x \leq 4.4, \text{ discharge}) \tag{1}$$

$$Li_xSn \rightarrow Sn + xLi^+ + xe^- \quad (0 < x \leq 4.4, \text{ charge}) \tag{2}$$

To specify the lithium storage mechanism of 3D-NPC@MTNPs electrode, the first three-cycle CVs were recorded at the voltage range of 0.01-1.5 V (vs. Li/Li^+) at a scan rate of 0.1 mV s^{-1}, as depicted in Fig. 4a. Clearly, in the first discharge process, there are two anodic peaks centered at 1.45 V and 0.2 V (vs. Li/Li^+), sequentially assigned to the formation of solid electrolyte interface (SEI) from the decomposition of organic electrolyte on the electrode surfaces, as well as the electrochemical alloying process of Sn indicated by Eq. (1).[30,35] Note that the typical SEI formed in the first lithiation process is a stable passivating layer over the electrode surfaces, and thus the corresponding electrochemical reaction is irreversible.[32,36] That means that the anodic peak at 1.45 V (vs. Li/Li^+) would no longer appear after the 1st cycle. Meanwhile, the two cathodic peaks centered at 0.78 V and 1.31 V (vs. Li/Li^+) in the first charge process can be observed respectively, which is mainly ascribed to the step-by-step electrochemical dealloying processes related to disassembly of Li_xSn $(0 < x \leq 4.4)$ alloy as described by Eq. (2). Additionally, it should be noted that the CV curve in the second cycle is nearly overlapped with the third one, indicating its excellent

electrochemical reversibility after the 1st cycle.

Fig. 4b shows the voltage vs. capacity profiles of 3D-NPC@MTNPs electrode ranging from 0.01 to 1.5 V (vs. Li/Li^+) at a current density of 0.1 mA cm^{-2}. As can be seen clearly, the 1st, 2nd and 3rd charge processes delivered the large reversible capacities of 0.485, 0.420 and 0.399 mAh cm^{-2}, respectively, with relatively high capacity retentions of 86.6% and 82.3%, implying its good structure stability during the lithiation-delithiation processes. Moreover, the difference between discharge and charge specific capacities is only 0.086 and 0.051 mAh cm^{-2} for the 2nd and 3rd cycles, indicative of its excellent electrochemical reversibility. Note that the 3rd discharge and charge curves overlapped well with those in the 2nd cycle, which is in good line with the CVs in Fig. 4a.

Fig. 4c exhibits the galvanostatic charge-discharge curve of 3D-NPC@MTNPs electrode at a current density of 0.1 mA cm^{-2}; for comparison, the counterpart of 2D-CF@TTFs electrode also was tested under the same condition. Evidently, both the 3D and 2D electrodes manifest an initial capacity decline in the first several cycles, which is closely related to the formation of SEI films consuming a mass of Li^+ and the partial irreversible conversion of Sn reacting with Li^+.[31] It should be noted, however, that compared to the continuous and fierce capacity decay of 2D-CF@TTFs electrode, the 3D-NPC@MTNPs electrode displays superior cycling stability and ultralong cycle life with 52.4% capacity retention after 500 cycles. Except for the first several cycles, its coulombic efficiency is always beyond 96.7%, which is, to the best of our knowledge, rarely seen for common LiM electrodes.[37,38] Impressively, the 3D porous

electrode delivers the much higher reversible capacities of 0.325, 0.259 and 0.256 mAh cm^{-2} than the 2D planar electrode (0.247, 0.097 and 0.056 mAh cm^{-2}) at the 10^{th}, 100^{th} and 250^{th} cycle, respectively. Even after 500 charge-discharge cycles, a relatively high charge specific capacity of 0.254 mAh cm^{-2} still can be reached, approximately 5 times greater than that of the 2D electrode with just 13.8% capacity retention after 250 cycles. The fast capacity loss of 2D-CF@TTFs electrode is mainly associated with the compactly layered stacking of Sn nanoparticles on the 2D planar substrate, which readily gives rise to the inadequate buffering of mechanical strain and even rapid detachment of active material during repeated lithiation-delithiation processes. In addition, we give a detailed comparison of lithium storage properties of the 3D-NPC@MTNPs electrode with other Sn-based electrode materials reported in the recent literature, as listed clearly in Table S2. Obviously, the markedly improved cycling stability and prolonged cycle life can be achieved smoothly in the 3D-NPC@MTNPs electrode.

Fig. 4d further illustrates the rate capability of 3D-NPC@MTNPs electrode, which is another important evaluation indicator for electrochemical performance of LIBs. As indicated expressly, the relatively large reversible capacities of 0.485, 0.391, 0.317 and 0.246 mAh cm^{-2} can be obtained after each 10 cycles at the current densities of 0.1, 0.2, 0.4 and 0.8 mA cm^{-2}, respectively. When the current density reverted to 0.1 mA cm^{-2} again, the reversible capacity enhanced to 0.4 mAh cm^{-2}, maintaining as high as ca. 82.5% capacity retention relative to that of the 10^{th} cycle at the same current density. Note that after enduring a series of high-rate lithiation-delithiation processes,

the reversible capacity still can reach 0.324 mAh cm^{-2} after 200 cycles, suggesting its outstanding rate capability. This can mainly put down to the intrinsic synergistic effect between unique 3D porous electrode configuration and good monodispersity of Sn nanoparticles that offers the essential benefits towards the ion and electron transport kinetics at the electrode/electrolyte and current collector/active material interfaces in LIBs, which will be discussed further based on EIS results in the following section.

In order to better understand the Li^+ and electron transport processes, the Nyquist plots of 3D-NPC@MTNPs and 2D-CF@TTFs electrodes before and after cyclings were measured, as depicted in Fig. 4e-f. Obviously, all Nyquist plots are composed of a compressed semicircle in the high-medium frequency region and an oblique line in the low frequency region. As well-known, the semicircle of high-medium frequency represents the charge transfer resistance (R_{ct}) associated with the electrochemical reactions occurring on electrode/electrolyte interfaces, while the oblique line of low frequency is closely related to the Li^+ diffusion coeffcient in electrode materials.[39] It is clear that the 3D-NPC@MTNPs electrode possesses significantly lower R_{ct} (ca. 65 Ω) in the pristine state than that of 2D-CF@TTFs electrode (ca. 300 Ω), implying its excellent electronic conductivity. Exhilaratingly, the R_{ct} of 3D-NPC@MTNPs electrode after 500 long-cycles can be identified to be ca. 105 Ω, slightly greater than its original value but far lower than that of 2D-CF@TTFs electrode just after 250 cycles (above 800 Ω), indicating the much better Li^+ and electron transport abilities in the 3D-NPC@MTNPs electrode. The fitting curves and equivalent circuits of EIS results of 3D-NPC@MTNPs and 2D-CF@TTFs electrodes after cyclings have been

carried out further, as presented in Fig. S3. As can be seen clearly, the R_{ct} of 3D-HP Sn-Ni electrode can be determined to be 106 Ω after 500 long-cycles, which is far lower than that of 2D-CF@TTFs electrode after 250 cycles (821 Ω). The present results clearly demonstrate that the unique architecture design (including bicontinuous 3D porous substrate, uniform distribution of Sn nanoparticles and good bonding force between them by chemical deposition) of 3D-NPC@MTNPs electrode is considerably beneficial to rapid Li^+ diffusion, electron transport and electrode/electrolyte wettability.

To further reveal the failure mechanisms of 3D-NPC@MTNPs and 2D-CF@TTFs electrodes, microstructure and surface micromorphology of the 3D and 2D electrodes after cyclings were examined, as shown in Fig. 5. For the 3D-NPC@MTNPs electrode, no severe structure damage and obvious detachment of active material can be observed from the electrode surfaces after 500 charge-discharge cycles, indicating the 3D porous electrode possesses good mechanical stability and bonding strength, which can effectively accommodate the huge structural strains and volume changes during repeated lithiation-delithiation processes. Note that the mean sizes of pores after cyclings seem to be smaller than their original state probably originating from residual organic electrolytes or related bi-products, which mainly are composed of the decomposition products of electrolyte with formation of protective films on the electrode surfaces and the reduction of some residual synthesis additives.[40] Moreover, the accumulative partial delithiation during cyclings can give rise to gradually coarsening of Sn nanoparticles and local shut down of porous window, preventing the

penetration of electrolyte and further reaction with tin inside, thus resulting in the gradual loss of capacity and slight fading of cycling performation. In contrast, the 2D-CF@TTFs electrode is subjected to severe structure collapse and ruin including extensive cracking and large-area detachment of tin just after 250 cyclic volume changes, as presented in Fig. 5c. The high-magnification SEM image further exhibits that except for the uneven cracks and pits, many irregular microclusters composed of varisized nanoparticles and nanoflakes can be seen clearly in Fig. 5d, which is in close connection with the rapid pulverization of tin caused by huge volume variation and insufficient structure cushion during repetitive charge-discharge processes. It is worth noting that the microstructure and surface micromorphology of the 2D planar electrode after cyclings have a significant difference from its initial state shown in Fig. 3e-f. Especially, the drastic reduction of tin content after cyclings clearly demonstrates the 2D planar substrate cannot accommodate the huge volume and structure variations effectively during repetitive lithiation-delithiation processes, eventually leading to the dreadful electrochemical properties.

Herein, the 3D-NPC@MTNPs//$LiCoO_2$ lithium ion full cell was assembled further by using the synthesized 3D porous composite as anode and commercial $LiCoO_2$ as cathode to effectively demonstrate its superiority for the practical application of LIBs. As indicated in Fig. 6, the electrochemcial properties of 3D-NPC@MTNPs//$LiCoO_2$ full cell were measured in the voltage range of 1.0-3.8 V. Fig. 6a shows the voltage vs. capacity profiles of 3D-NPC@MTNPs//$LiCoO_2$ full cell at a current density of 0.1 mA cm^{-2}. Clearly, the 1^{st}, 2^{nd} and 3^{rd} discharge processes (Li^+ migration from

3D-NPC@MTNPs to $LiCoO_2$) delivered the relatively large reversible capacities of 1.111, 1.224 and 1.293 mAh cm^{-2}, respectively. Note that the discharge specific capacity increases slightly from the 1st to 3rd cycle primarily due to the occurrence of electrode activation in the initial several cycles from the full permeation of electrolyte into the 3D nanostructured electrode. Moreover, the charge capacity curve of 2nd cycle overlapped well with that of the 3rd cycle, suggesting the good electrochemical reversibility. Fig. 6b exhibits the cycle performance of 3D-NPC@MTNPs//$LiCoO_2$ full cell at a current density of 0.1 mA cm^{-2}. Similarly, a slight increase for reversible capacity can be observed in the first three cycles. After the short activation processes, the 3D-NPC@MTNPs//$LiCoO_2$ full cell displayed the good cycling stability and long cycle life with 94.9% capacity retention after 50 cycles, indicating its excellent ability in charge-discharge cycling. Excitingly, a high discharge capacity of 0.815 mAh cm^{-2} still can be reached after 100 cycles, maintaining as high as 73.4% capacity retention. Typically, a digital image of the light-emitting-diode lightened by the assembled full cell with full-charged state after 100 cycles was presented further in the inset in Fig. 6b, clearly demonstrating the favorable availability of 3D-NPC@MTNPs composite towards household/industrial microelectronic devices.

Compared to the 2D-CF@TTFs, the excellent electrochemical performance of the 3D-NPC@MTNPs electrode demonstrates the inherent merits of synergistic effect between unique 3D porous electrode architecture inherited from current collector by dealloying and favorable monodispersity of single-crystal Sn nanoparticles through low-temperature chemical deposition, which can be rationalized detailedly as follows:

(1) The 3D nanoporous structure with large specific surface area can reduce Li^+ diffusion length remarkably between electrode and electrolyte. (2) The unique electrode architecture with open, bicontinuous interpenetrating porous network can provide high-efficient electron transport pathways.[21,41] (3) The adequate room amongst tin nanoparticles can accommodate huge volume change during repeated charge-discharge processes.[42,43] (4) The tin nanoparticles with good monodispersity and ultrafine particle size can offer more active sites reacting with Li^+ in the electrolyte and meanwhile bring about smaller mechanical strain associated with volume expansion during lithiation reactions.[44] (5) The good binding force between active material and current collector by chemical deposition can effectively prevent active material from cracking, pulverization and rapid detachment from current collector, resulting in the good structure stability. (6) The use of no additional binders and conductive agents can further improve the energy and power densities as it is assembled into full cells. Besides, the electroless plating technique possesses the evident advantages of simplicity, low cost and being applicable for large-scale synthesis, which might be used in production to make it competitive in technology and economy in the near future. Thus, we believe that this present work provides an expected possibility towards the practical application of metal based anode materials with high theoretical capacity in LIBs.

4. Conclusions

In summary, we develop a facile low-temperature synthesis protocol to construct the monolithic 3D nanoporous copper-supported monodispersed tin nanoparticles

without additional binder and conductive agents, in which active tin particles possess the typical sizes of 6±2 nm and single crystal nature. The freestanding 3D-NPC with pore sizes of ca. 200 nm, acting as both current collector and substrate of tin, can be obtained easily by chemical dealloying of as-cast Al 45 at.% Cu alloy sheets in a diluted acidic solution at an elevated temperature. The 3D-NPC@MTNPs composite can be fabricated massively by electroless plating Sn on the 3D-NPC substrate in an acidic plating bath at the low temperature. Compared to the 2D-CF@TTFs, the 3D-NPC@MTNPs composite as anode for LIBs exhibits the markedly higher first reversible capacity of 0.485 mAh cm^{-2} as well as excellent cycling stability with 52.4% capacity retention and > 96.7% coulombic efficiency upon 500 cycles, which can be mainly attributed to the synergistic effect between unique 3D nanoporous electrode configuration and benign monodispersity of single-crystal Sn nanoparticles facilitating the alleviation of volume change and mechanical strain, improvement of structural integrity and stability, enhancement of active sites and bonding force, optimization of ion and electron migration paths, suggesting a considerably promising application in high-performance LIBs.

Acknowledgements

We give thanks to financial support by the National Natural Science Foundation of China (51604177), the State Key Basic Research Program of PRC (2013CB934001), the Research Grants Council of the Hong Kong Special Administrative Region, China (GRF PolyU152174/17E), the Hong Kong Scholars Program (XJ2014045, G-YZ67), the China Postdoctoral Science Foundation (2015M570784), the International S&T

Cooperation and Exchange Program of Sichuan Province (2017HH0068), the Scientific Research Fund of Sichuan Provincial Department of Education (16ZB0002), the Experimental Technology Project of Sichuan University (20170133), the “1000 Talents Plan” of Sichuan Province, the Fundamental Research Funds for the Central Universities, and the Talent Introduction Program of Sichuan University (YJ201410).

References

1 J. M. Tarascon and M. Armand, *Nature,* 2001, **414***,* 359－367.

2 M. Armand and J. M. Tarascon, *Nature,* 2008, **451,** 652－657.

3 T. Brousse, O. Crosnier, X. Devaux, P. Paillard, J. Santos-Pena and D. M. Schleich, *Powder Technol.,* 2002, **128,** 124－130.

4 M. H. Park, M. G. Kim, J. Joo, K. Kim, J. Kim, S. Ahn, Y. Cui and J. Cho, *Nano Lett.,* 2009, **9,** 3844－3847.

5 M. Winter and J. O. Besenhard, *Electrochim. Acta,* 1999, **45,** 31－50.

6 G. X. Wang, J. H. Ahn, J. Yao, S. Bewlay and H. K. Liu, *Electrochem. Commun.,* 2004, **6,** 689－341.

7 K. D. Kepler, J. T. Vaughey and M. M. Thackeray, *J. Power Sources,* 1999, **81－82,** 383－387.

8 A. H. Whitehead, J. M. Elliott and J. R. Owen, *J. Power Sources,* 1999, **81－82,** 33－38.

9 J. Yang, M. Wachtler, M. Winter and J. O. Besenhard, *Electrochem. Solid-State Lett.,* 1999, **2,** 161－163.

10 H. Li, X. J. Huang, L. Q. Chen, Z. G. Wu and Y. Liang, *Electrochem. Solid-State*

Lett., 1999, **2,** 547－549.

11 Z. P. Guo, J. Z. Wang, H. K. Liu and S. X. Dou, *J. Power Sources,* 2005, **146,** 448－451.

12 M. Valvo, U. Lafont, D. Munao and E. M. Kelder, *J. Power Sources,* 2009, **189,** 297－302.

13 W. Choi, J. Y. Lee, B. H. Jung and H. S. Lim, *J. Power Sources,* 2004, **136,** 154－159.

14 Y. Hu, Y. Guo, W. Sigle, S. Hore, P. Balaya and J. Maier, *Nat. Mater.,* 2006, **5,** 713.

15 O. Mao, R. L. Turner, I. A. Courtney, B. D. Fredericksen, M. I. Buckett, L. J. Krause and J. R. Dahn, *Electrochem. Solid-State Lett.,* 1999, **2,** 3－5.

16 A. Trifonova, M. Wachtler, M. R. Wagner, H. Schriettner, C. Mitterbauer, F. Hofer, K. C. Möller, M. Winter and J. O. Besenhard, *Solid State Ionics,* 2004, **168,** 51－59.

17 M. Yoshio, T. Tsumura and N. Dimov, *J. Power Sources,* 2006, **146,** 10－14.

18 J. Y. Xiang, J. P. Tu, X. L.Wang, X. H. Huang, Y. F. Yuan, X. H. Xia and Z. Y. Zeng, *J. Power Sources,* 2008, **185,** 519－525.

19 C. Arbizzani, S. Beninati, M. Lazzari and M. Mastragostino, *J. Power Sources,* 2005, **141,** 149－155.

20 Y. Yu, C. H. Chen and J. L. Shui, *Angew. Chem. Int. Ed.* 2005, **44,** 7085－7089.

21 H. Zhang, X. Yu and P. V. Braun, *Nat. Nanotechnol,* 2011, **6,** 277－281.

22 T. Jiang, S. Zhang, X. Qiu, W. Zhu and L. Chen, *J. Power Sources,* 2007, **166,** 503－508.

23 T. Jiang, S. Zhang, X. Qiu, W. Zhu and L. Chen, *Electrochem. Commun.,* 2007, **9,**

930－934.

24 Y. Yu, L. Gu, X. Y. Lang, C. B. Zhu, T. Fujita, M. W. Chen and J. Maier, *Adv. Mater.,* 2011, **23,** 2443－2447.

25 Y. Yu, L. Gu, X. Y. Lang, C. B. Zhu, T. Fujita, M. W. Chen and J. Maier, *Adv. Energy Mater.,* 2013, **3,** 281－285.

26 M. C. Dixon, T. A. Daniel, M. Hieda, D. M. Smilgies, M. H. W. Chan and D. L. Allara, *Langmuir,* 2007, **23,** 2414－2422.

27 K. Sieradzki, R. R. Corderman and K. Shukla, *Phil. Mag. A,* 1989, **59,** 713－746.

28 S. C. Zhang, Y. L. Xing, T. Jiang, Z. J. Du, F. Li, L. He and W. B. Liu, *J. Power Sources,* 2011, **196,** 6915－6919.

29 Z. Luo, J. C. Xu, B. Yuan, H. Li, R. Z. Hu, L. C. Yang, Y. Gao and M. Zhu, *Mater. Lett.,* 2018, **213,** 189－192.

30 Z. Luo, J. C. Xu, B. Yuan, R. Z. Hu, L. C. Yang, Y. Gao and M. Zhu, *ACS Appl. Mater. Inter.,* 2018, **10,** 22050－22058.

31 Z. J. Du, S. C. Zhang, T. Jiang and Z. M. Bai, *Electrochim. Acta,* 2010, **55,** 3537－3541.

32 M. O. Guler, M. Guzeler, D. Nalci, M. Singil, E. Alkan, M. Dogan, A. Guler and H. Akbulut, *Appl. Surf. Sci.,* 2018, **446,** 122－130.

33 X. Dong, W. B. Liu, X. Chen, J. Z. Yan, N. Li, S. Q. Shi, S. C. Zhang and X. S. Yang, *Chem. Eng. J.,* 2018, **350,** 791－798.

34 M. Mayo and A. J. Morris, *Chem. Mater.,* 2017, **29,** 5787－5795.

35 M. Inaba, T. Uno and A. Tasaka, *J. Power Sources,* 2005, **146,** 473－477.

36 Y. Xing, S. Wang, B. Fang, Y. Feng and S. Zhang, *Micropor. Mesopor. Mat.,* 2018, **261,** 237－243.

37 J. Hassoun, S. Panero, P. Simon, P.-L. Taberna and B. Scrosati, *Adv. Mater.,* 2007, **19,** 1632－1635.

38 J. Hassoun, G. Derrien, S. Panero and B. Scrosati, *Adv. Mater.,* 2008, **20,** 3169－3175.

39 M. Uysal, T. Cetinkaya, A. Alp and H. Akbulut, *J. Alloys Compd.,* 2015, **645,** 235－242.

40 D. Aurbach, B. Markovsky, M. D. Levi, E. Levi, A. Schechter, M. Moshkovich and Y. Cohen, *J. Power Sources,* 1999, **81-82,** 95－111.

41 L. Bao, J. Zang and X. Li, *Nano Lett.,* 2011, **11,** 1215－1220.

42 L. F. Cui, Y. Yang, C. M. Hsu and Y. Cui, *Nano Lett.,* 2009, **9,** 3370－3374.

43 J. Yang, J. M. Zhang, X. Y. Zhou, R. P. Ren, M. Jiang and J. J. Tang, *ACS Appl. Mater. Inter.*, 2018, **10,** 35216－35223.

44 W. B. Liu, S. C. Zhang, N. Li, S. S. An and J. W. Zheng, *Int. J. Electrochem. Sci.,* 2013, **8,** 347－358.

Figure Captions

Figure 1. The schematic illustration showing the preparation process of the freestanding 3D-NPC@MTNPs composite.

Figure 2. XRD patterns of (a) 3D-NPC substrate by chemical dealloying of the Al-Cu alloy in the HCl solution, 3D-NPC@MTNPs composite after electroless plating tin on the 3D-NPC substrate at the low temperature, and (b) 2D-CF@TTFs composite after electroless plating tin on the 2D-CF substrate at the low temperature.

Figure 3. SEM images showing the microstructures of (a,b) 3D-NPC substrate by chemical dealloying of the Al 45 at.% Cu alloy sheets in the 5 wt.% HCl solution at 90℃ for 5 hrs, (c,d) 3D-NPC@MTNPs and (e,f) 2D-CF@TTFs composites after electroless plating tin at the low temperature, in which parts b, d and f are the high-magnification images. Insets of parts a, c and e are the corresponding chemcial compositions. (g) TEM image shows the surface micromorphology of 3D-NPC@MTNPs composite after the electroless plating tin. (h) HRTEM image shows the different lattice fringes on the ligament surface corresponding to NPC substrate and Sn nanoparticle, respectively. Broken line indicates the boundary between NPC substrate and Sn nanoparticles.

Figure 4. (a) CVs of 3D-NPC@MTNPs electrode for the first three cycles ranging from 0.01 to 1.5 V (vs. Li/Li^+) at a scan rate of 0.1 mV s^{-1}. (b) Voltage vs. capacity profiles of 3D-NPC@MTNPs electrode at a current density of 0.1 mA cm^{-2}. (c) Cycle performance curves of 3D-NPC@MTNPs and 2D-CF@TTFs electrodes at a current density of 0.1 mA cm^{-2}. (d) Rate capability profiles of 3D-NPC@MTNPs electrode at

different current densities of 0.1, 0.2, 0.4, 0.8 mA cm^{-2}. (e-f) Nyquist plots of 3D-NPC@MTNPs and 2D-CF@TTFs electrodes before and after cyclings. The insets in parts e and f display the corresponding high frequency zones at a higher magnification.

Figure 5. SEM images showing the microstructures of (a,b) 3D-NPC@MTNPs electrode after 500 charge-discharge cycles and (c,d) 2D-CF@TTFs electrode after 250 charge-discharge cycles. Insets of parts a and c are the corresponding chemcial compositions.

Figure 6. (a) Voltage vs. capacity profiles of 3D-NPC@MTNPs//$LiCoO_2$ full cell at a current density of 0.1 mA cm^{-2}; (b) Cycle performance curves of 3D-NPC@MTNPs//$LiCoO_2$ full cell at a current density of 0.1 mA cm^{-2}, in which the inset shows a digital image of the light-emitting-diode lightened by the assembled full cell with full-charged state after 100 cycles.

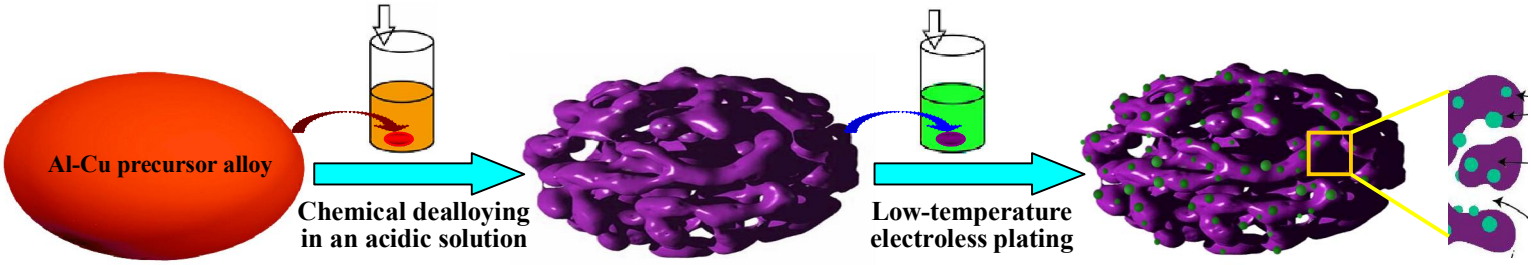

Figure 1. The schematic illustration showing the preparation process of the freestanding 3D-NPC@MTNPs composite.

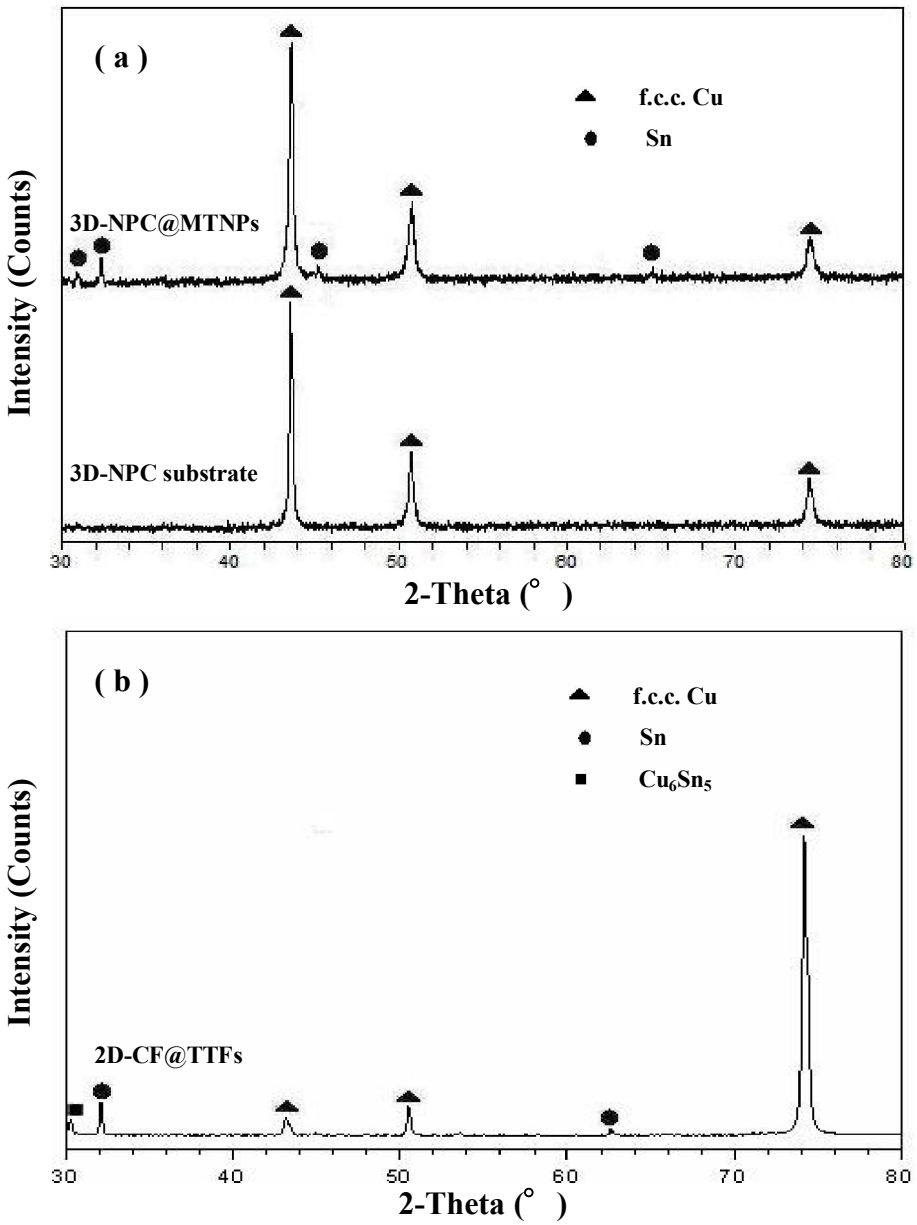

Figure 2. XRD patterns of (a) 3D-NPC substrate by chemical dealloying of the Al-Cu alloy in the HCl solution, 3D-NPC@MTNPs composite after electroless plating tin on the 3D-NPC substrate at the low temperature, and (b) 2D-CF@TTFs composite after electroless plating tin on the 2D-CF substrate at the low temperature.

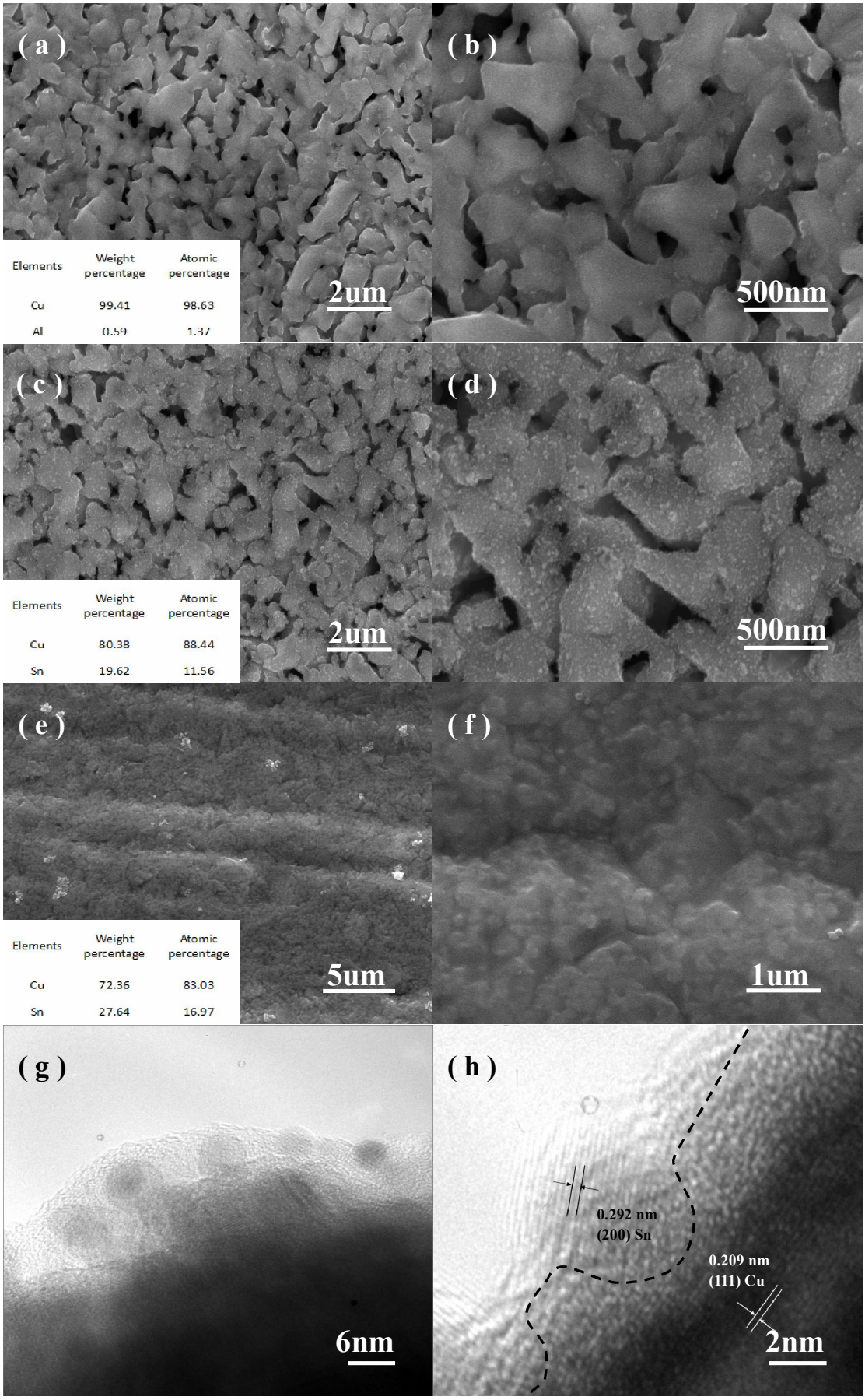
(a)
Elements Weight percentage Atomic percentage
Cu 99.41 98.63
Al 0.59 1.37
2um
(b)
500nm
(c)
Elements Weight percentage Atomic percentage
Cu 80.38 88.44
Sn 19.62 11.56
2um
(d)
500nm
(e)
Elements Weight percentage Atomic percentage
Cu 72.36 83.03
Sn 27.64 16.97
5um
(f)
1um
(g)
6nm
(h)
0.292 nm
(200) Sn
0.209 nm
(111) Cu
2nm

Figure 3. SEM images showing the microstructures of (a,b) 3D-NPC substrate by chemical dealloying of the Al 45 at.% Cu alloy sheets in the 5 wt.% HCl solution at 90℃ for 5 hrs, (c,d) 3D-NPC@MTNPs and (e,f) 2D-CF@TTFs composites after electroless plating tin at the low temperature, in which parts b, d and f are the high-magnification images. Insets of parts a, c and e are the corresponding chemcial compositions. (g) TEM image shows the surface micromorphology of 3D-NPC@MTNPs composite after the electroless plating tin. (h) HRTEM image shows the different lattice fringes on the ligament surface corresponding to NPC substrate and Sn nanoparticle, respectively. Broken line indicates the boundary between NPC substrate and Sn nanoparticles.

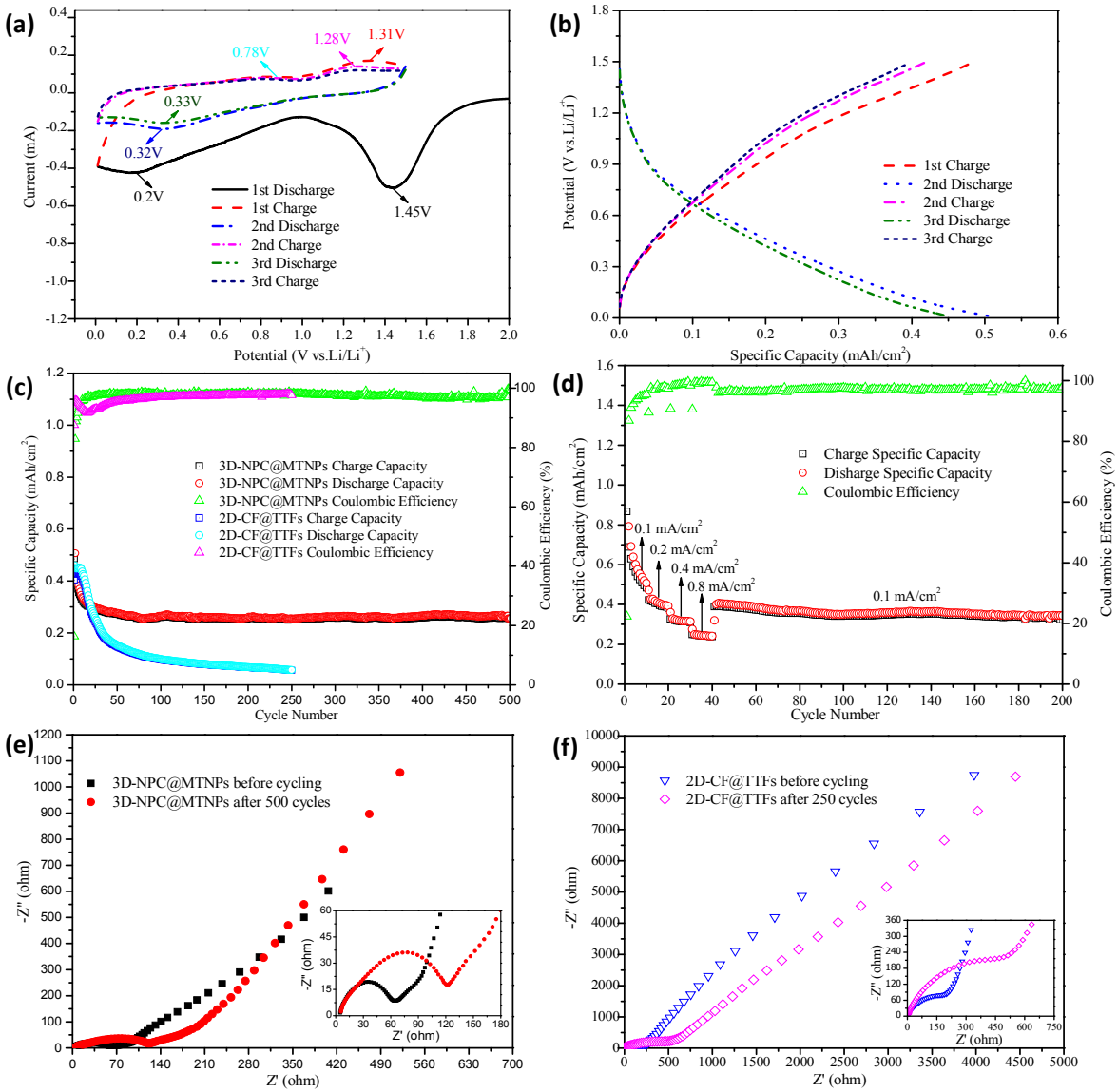

Figure 4. (a) CVs of 3D-NPC@MTNPs electrode for the first three cycles ranging from 0.01 to 1.5 V (vs. Li/Li^+) at a scan rate of 0.1 mV s^{-1}. (b) Voltage vs. capacity profiles of 3D-NPC@MTNPs electrode at a current density of 0.1 mA cm^{-2}. (c) Cycle performance curves of 3D-NPC@MTNPs and 2D-CF@TTFs electrodes at a current density of 0.1 mA cm^{-2}. (d) Rate capability profiles of 3D-NPC@MTNPs electrode at different current densities of 0.1, 0.2, 0.4, 0.8 mA cm^{-2}. (e-f) Nyquist plots of 3D-NPC@MTNPs and 2D-CF@TTFs electrodes before and after cyclings. The insets in parts e and f display the corresponding high frequency zones at a higher magnification.

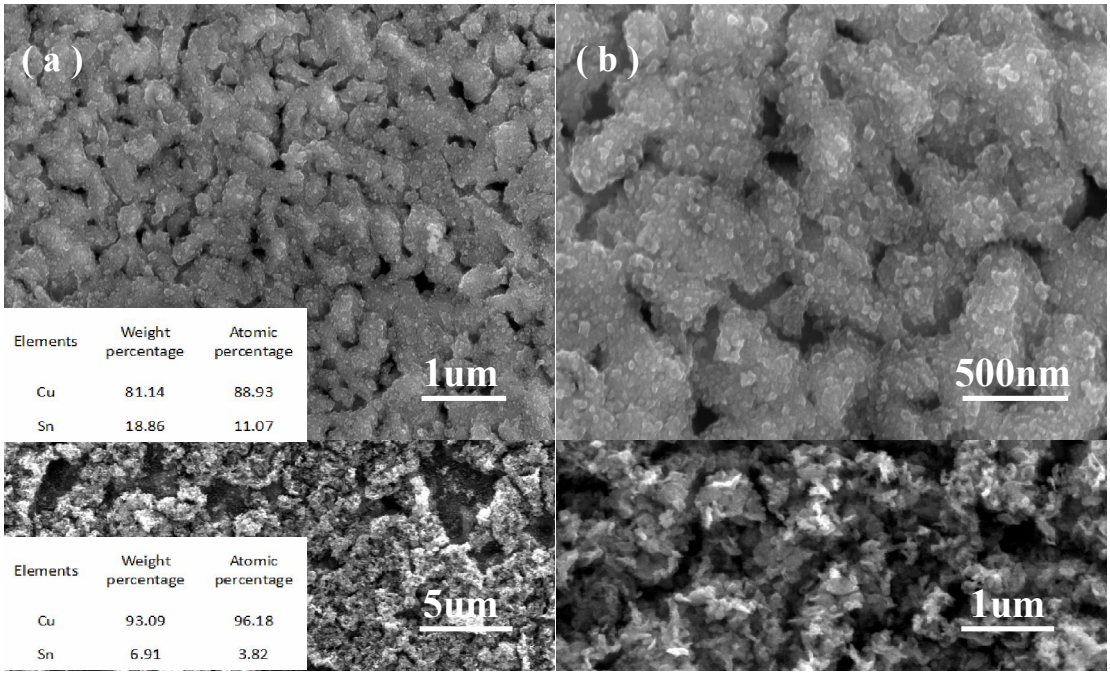

Figure 5. SEM images showing the microstructures of (a,b) 3D-NPC@MTNPs electrode after 500 charge-discharge cycles and (c,d) 2D-CF@TTFs electrode after 250 charge-discharge cycles. Insets of parts a and c are the corresponding chemcial compositions.

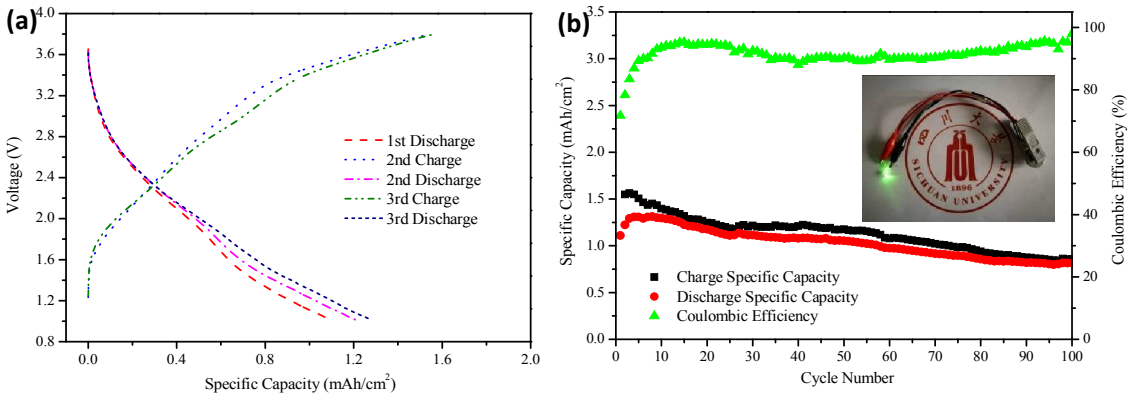

Figure 6. (a) Voltage vs. capacity profiles of 3D-NPC@MTNPs//$LiCoO_2$ full cell at a current density of 0.1 mA cm^{-2}; (b) Cycle performance curves of 3D-NPC@MTNPs//$LiCoO_2$ full cell at a current density of 0.1 mA cm^{-2}, in which the inset shows a digital image of the light-emitting-diode lightened by the assembled full cell with full-charged state after 100 cycles.